

TECHNICAL REPORTS: METHODS

10.1029/2019GC008273

Key Points:

- Oxygen fugacity (fO_2) is a fundamental thermodynamic property that governs the redox potential in solid Earth systems
- Specialized software, Geo- fO_2 , was developed for analysis of magmatic fO_2
- With user-friendly interfaces, Geo- fO_2 is easy to input files, output data in Excel files, and plot results as binary diagrams

Supporting Information:

- Supporting Information S1
- Table S1
- Table S2
- Table S3
- Table S4
- Table S5
- Table S6
- Table S7
- Table S8
- Table S9
- Table S10
- Figure S1
- Figure S2

Correspondence to:

Z. Yang,
zm.yang@hotmail.com

Citation:



Li, W., Cheng, Y., & Yang, Z. (2019). Geo- fO_2 : Integrated software for analysis of magmatic oxygen fugacity. *Geochemistry, Geophysics, Geosystems*, 20. <https://doi.org/10.1029/2019GC008273>

Received 18 FEB 2019

Accepted 11 APR 2019

Accepted article online 23 APR 2019

Geo- fO_2 : Integrated Software for Analysis of Magmatic Oxygen Fugacity

Weikai Li^{1,2,3}, Yuanqi Cheng⁴ , and Zhiming Yang^{1,5} 

¹Key Laboratory of Deep-Earth Dynamics, Institute of Geology, Chinese Academy of Geological Sciences, Beijing, China, ²School of Earth and Space Sciences, Peking University, Beijing, China, ³Department of Earth Sciences, University of Geneva, Geneva, Switzerland, ⁴Institute of Ocean Research, Peking University, Beijing, China, ⁵Economic Geology Research Centre (EGRU), College of Science and Engineering, James Cook University, Townsville, Queensland, Australia

Abstract Oxygen fugacity (fO_2) is a fundamental thermodynamic property governing redox potential in solid Earth systems. Analysis of magmatic fO_2 aids our understanding of the valence state and solubility of multivalent elements during magma evolution. Specialized software, Geo- fO_2 , was developed for calculating magmatic fO_2 on the basis of oxybarometers and thermobarometers for common minerals (amphibole, zircon, and biotite) in intermediate-silicic magmas. With user-friendly interfaces, it is easy to input files (.csv or Excel files), output data in Excel files, and plot results as binary diagrams that can be saved as vector graphics and modified using image-processing software.

1. Introduction

Oxygen fugacity (fO_2) is defined as the partial pressure of oxygen within a system (e.g., Carmichael, 1991; Frost, 1991; Lee et al., 2005) and is a fundamental thermodynamic property governing redox potential in solid Earth systems. In particular, during magma evolution the fO_2 controls valence states of multivalent elements (e.g., Fe, Cu, Au, V, S, and C), which in turn controls their crystal/melt partitioning (e.g., Brounce et al., 2014; Canil, 2002) and solubility in silicate magmas (e.g., Carmichael, 1991; Evans & Tomkins, 2011; Rowe et al., 2009). This is particularly crucial for ore mineralization in magmatic-hydrothermal systems (e.g., porphyry-type deposits; Jugo, 2009; Richards, 2015; Sillitoe, 2010; Simon & Ripley, 2011; Yang et al., 2016; Zajacz et al., 2011) and speciation of volatiles during magma degassing (e.g., Burgisser & Scaillet, 2007; Clémente et al., 2004; Iacono-Marziano et al., 2012; Jugo et al., 2005; Mathez, 1984; Moretti & Ottonello, 2005; Pawley et al., 1992).

Two early models for the calculation of magmatic fO_2 involved bulk Fe^{3+}/Fe^{2+} (or $Fe^{3+}/\Sigma Fe$) ratios (e.g., Kennedy, 1948; Kilinc et al., 1983; Kress & Carmichael, 1991; Sack et al., 1981) and the Fe-Ti oxide oxybarometer (e.g., Andersen & Lindsley, 1985; Buddington & Lindsley, 1964; Carmichael, 1966; Ghiorso & Sack, 1991). Corresponding programs include QUILF (Andersen et al., 1993), MELTS (Ghiorso et al., 2002; Ghiorso & Sack, 1995; Smith & Asimow, 2005), ILMAT (Lepage, 2003), and Petrolog3 (Danyushevsky & Plechov, 2011). However, bulk Fe^{3+}/Fe^{2+} ratios in rocks are highly susceptible to alteration by weathering, hydrothermal modification, and degassing and also susceptible to early fractional crystallization of mafic minerals (e.g., olivine; Cottrell & Kelley, 2011). The Fe-Ti oxide oxybarometer is limited to magmas that precipitate both ilmenite and magnetite solid-solution during cooling. Additionally, Fe-Ti oxides tend to reequilibrate at subsolidus temperatures during slow cooling or due to hydrothermal alteration (Venezky & Rutherford, 1999). Consequently, the oxybarometer is typically applied to volcanic rather than intrusive systems.

Recently, some new mineral oxybarometers have been calibrated on the basis of the composition of relatively stable and common minerals, which are often found in intermediate-silicic magmas, such as zircon (Ballard et al., 2002; Burnham & Berry, 2012; Smythe & Brennan, 2016; Trail et al., 2011, 2012, 2015) and amphibole (Ridolfi et al., 2010; Ridolfi & Renzulli, 2012). These oxybarometers, plus previously calibrated oxybarometers for other minerals (e.g., biotite; Wones, 1972, 1981; Wones & Eugster, 1965), make it possible to track initial magmatic fO_2 and its subsequent variations (e.g., Li et al., 2019). A few programs developed for individual minerals are available for simple estimations of magmatic fO_2 (e.g., Ridolfi et al., 2010; Yavuz, 2003a, 2003b; Yavuz & Öztaş, 1997); however, specialized software integrating previously and recently calibrated oxybarometers that can systematically calculate and visualize magmatic fO_2 is lacking.

In this study, we developed user-friendly interfaces for the first version of integrated software, “Geo- fO_2 ,” written in Python (van Rossum & Drake, 1995, 2011). Geo- fO_2 includes oxybarometers and thermobarometers of zircon (Ferry & Watson, 2007; Miller et al., 2003; Trail et al., 2011; Watson & Harrison, 1983), amphibole (Ridolfi et al., 2010; Schmidt, 1992), and biotite (Henry et al., 2005; Uchida et al., 2007; Wones, 1972). It is designed to (1) calculate cations in minerals; (2) calculate thermodynamic parameters of magma (e.g., fO_2 , temperature, and pressure) during magma ascent and fractional crystallization; and (3) visualize calculated results through a plotting interface.

2. Methods

2.1. Amphibole Oxybarometer, Thermobarometer, and Hygrometer

Amphibole is an important mineral in hydrous magmas and is stable across a wide P - T range (700–1100 °C; 0.1–25 kbar; Allen & Boettcher, 1978; Eggler, 1972; Nandedkar et al., 2014). Based on electron microprobe analysis (EMPA) data of amphibole, Ridolfi et al. (2010) produced the ΔNNO - Mg^* oxybarometer (ΔNNO is the deviation of $\log fO_2$ from the Ni-NiO buffer [NNO; O'Neill & Pownceby, 1993]), Si^* -sensitive thermometer, Al_T -sensitive barometer, and $^{VI}Al^*$ -sensitive hygrometer to estimate fO_2 , temperature, pressure, and H_2O contents of magma, respectively, from which amphibole crystallizes, as described by the following formulae:

$$\Delta NNO = (1.644 \times Mg^*) - 4.01 \quad (\sigma_{est} = \pm 0.22 \text{ log unit}), \quad (1)$$

where $Mg^* = Mg + (Si/47) - (Al^{VI}/9) - (1.3 \times Ti^{VI}) + (Fe^{3+}/3.7) + (Fe^{2+}/5.2) - ({}^B Ca/20) - ({}^A Na/2.8) + ((1 - {}^A Na - {}^A K)/9.5)$; Mg , Si , Al^{VI} , Ti^{VI} , Fe^{3+} , and Fe^{2+} represent the number of atoms of each per formula unit based on 13 cations; Al^{VI} and Ti^{VI} are the numbers of Al and Ti atoms in octahedral sites; ${}^A Na$ and ${}^A K$ are the Na and K contents of A sites; and ${}^B Ca$ is the Ca content of B sites. The σ_{est} represents the standard error of the calibration (Ridolfi et al., 2010); the same below.

$$T \text{ (}^\circ\text{C)} = (-151.487 \times Si^*) + 2041 \quad (\sigma_{est} = \pm 22 \text{ }^\circ\text{C}), \quad (2)$$

where $Si^* = Si + (Al^{IV}/15) - (2 \times Ti^{IV}) - (Al^{VI}/2) - (Ti^{VI}/1.8) + (Fe^{3+}/9) + (Fe^{2+}/3.3) + (Mg/26) + ({}^B Ca/5) + ({}^B Na/1.3) - ({}^A Na/15) + ((1 - {}^A Na - {}^A K)/2.3)$; Al^{IV} and Ti^{IV} are the numbers of Al and Ti atoms in tetrahedral sites; ${}^B Na$ is the Na content of B sites.

$$P \text{ (kbar)} = 0.19209 \times e^{(1.438 Al_T)} \quad (\sigma_{est} = \pm 0.54 \text{ kbar}), \quad (3)$$

where Al_T is the total number of Al atoms per amphibole unit formula.

$$H_2O \text{ (wt.}\%) = (5.215 \times {}^{VI}Al^*) + 12.28 \quad (\sigma_{est} = \pm 0.4 \text{ wt.}\%), \quad (4)$$

where ${}^{VI}Al^* = Al^{VI} + (Al^{IV}/13.9) - ((Si + Ti^{VI})/5) - ({}^C Fe^{2+}/3) - (Mg/1.7) + (({}^B Ca + 1 - {}^A Na - {}^A K)/1.2) + ({}^A Na/2.7) - (1.56 \times {}^A K) - (Fe\#/1.6)$; ${}^C Fe^{2+}$ is the Fe^{2+} content of C sites; $Fe\# = Fe^{3+}/(Fe^{3+} + Fe^{2+} + Mg + Mn)$.

The classical Al-in-amphibole barometer of Schmidt (1992) is also provided:

$$P \text{ (kbar)} = -3.01 + (4.76 \times Al_T) \quad (\sigma_{est} = \pm 0.6 \text{ kbar}), \quad (5)$$

where Al_T is the total number of Al atoms per amphibole unit formula.

2.2. Zircon Oxybarometer, Thermometer, and Ce^{4+}/Ce^{3+} Ratios

Zircon is an exceptionally durable mineral that retains primary chemistry for most elements and isotopes from the time of its igneous crystallization (Cherniak et al., 1997). Zircon saturation temperature can be obtained by using the Zr saturation thermometer of Watson and Harrison (1983):

$$\ln D_{Zr}^{zircon/melt} = -3.8 - (0.85 \times (M - 1)) + (12,900 / (T + 273.15)), \quad (6)$$

where $D_{Zr}^{zircon/melt}$ is the Zr concentration ratio between zircon and melt, T is temperature (°C), and $M = (Na + K + 2Ca)/(Al \times Si)$ is the cation ratio of the bulk components. If the Zr contents of zircons are unknown, an approximate content of 496,000 ppm is used for magmatic zircons (Miller et al., 2003).

Another revised Ti-in-zircon thermometer (Ferry & Watson, 2007) allows calculation of zircon crystallization temperature (°C) using the Ti content (ppm) of zircon (Ti_{zircon}) and activities of SiO_2 (a_{SiO_2}) and TiO_2 (a_{TiO_2}) in host melt:

$$\log Ti_{\text{zircon}} = (5.711 \pm 0.072) - (4,800 \pm 86) / (T + 273.15) - \log a_{SiO_2} + \log a_{TiO_2}. \quad (7)$$

For quartz-saturated melts, a_{SiO_2} is set to 1.0, and a_{TiO_2} can be estimated using the activity model of Ghiorso and Gualda (2013). In Geo-fO₂, a manual input box allows the user to input appropriate values of a_{SiO_2} and a_{TiO_2} as described in section 3.

Trail et al. (2011) provided a zircon oxybarometer for determining the redox state of magmas based on the Ce anomaly in zircon. The Ce anomaly is defined as the degree to which the calculated Ce partition coefficient differs from that expected based on partition coefficients of its neighboring elements, La and Pr. It is expressed as $(Ce/Ce^*)_D$

$$(Ce/Ce^*)_D = D_{Ce}^{\text{zircon/melt}} / \left(D_{La}^{\text{zircon/melt}} \times D_{Pr}^{\text{zircon/melt}} \right)^{1/2}, \quad (8)$$

$$\ln (Ce/Ce^*)_D = (0.1156 \pm 0.0050 \times \ln fO_2) + ((13,860 \pm 708) / (T + 273.15)) - (6.15 \pm 0.484), \quad (9)$$

where $D_{Ce}^{\text{zircon/melt}}$, $D_{La}^{\text{zircon/melt}}$, and $D_{Pr}^{\text{zircon/melt}}$ are partition coefficients of Ce, La, and Pr between zircon and melt, respectively, and T is temperature (°C). If components of the melt are not available, bulk components of host rock are allowed to be used as an alternative.

However, the accurate determination of Ce anomalies based on La and Pr contents is often problematic due to the low La and Pr concentrations in zircon (e.g., Dilles et al., 2015; Qiu et al., 2013; Trail et al., 2012; Wang et al., 2014). Studies of natural zircon/melt partitioning have suggested that it can be reasonably assumed that $(Ce/Ce^*)_D \approx (Ce/Ce^*)_{CHUR}$ (e.g., Hinton & Upton, 1991; Sano et al., 2002; Thomas et al., 2002). However, Ce anomaly in the melt during zircon crystallization may have been influenced by some magmatic processes, that is, calculated $(Ce/Ce^*)_{CHUR}$ values may be overestimated under oxidized conditions due to fractional crystallization (e.g., monazite; Skora & Blundy, 2010; Stepanov et al., 2012) or contamination (Elderfield et al., 1981; Trail et al., 2012). As an alternative, the lattice-strain model (LSM; Blundy & Wood, 1994) may be used to estimate zircon Ce anomalies (expressed as $(Ce/Ce^*)_{LSM}$) using more enriched rare Earth elements (REEs; e.g., Nd, Sm, and Gd–Lu; Qiu et al., 2013; Trail et al., 2012) with better statistics (Burnham & Berry, 2012; Smythe & Brenan, 2016; Zou et al., 2019). $(Ce/Ce^*)_D$ was therefore set at $(Ce/Ce^*)_D = (Ce/Ce^*)_{LSM}$ for Ce anomalies in this study. Specifically, the partition coefficient of cation i between zircon and melt is related to the lattice-strain energy created by substituting a cation with an ionic radius (r_i) different to the optimal value for that site (r_0 ; Blundy & Wood, 1994). The corresponding expression is

$$\ln D_i = \ln D_0 - (4\pi \times E \times N_A \times (r_i/3 + r_0/6) \times (r_i - r_0)^2) / (R \times (T + 273.15)), \quad (10)$$

where D_0 is the strain-compensated partition coefficient, E is Young's modulus, N_A is Avogadro's number, R is the gas constant, and T is temperature (°C). Plotting $\ln D_i$ versus the term $(r_i/3 + r_0/6) \times (r_i - r_0)^2$ yields a linear relationship for isoivalent series of cations. If the ionic radii of Ce^{4+} and Ce^{3+} are known, their partition coefficients can be determined by interpolation (see also in Smythe & Brenan, 2016). The value of $D_{Ce}^{\text{zircon/melt}}$ lies between the partition coefficients of the two valence-state end-members (Ce^{4+} and Ce^{3+}), and the magmatic fO_2 can be determined by combination of equations (8) and (9). REE ionic radii were taken from Shannon (1976).

Zircon Ce^{4+}/Ce^{3+} ratios (Ballard et al., 2002) offer another method for estimating magma redox states. The ionic radius of Ce^{4+} (0.87 Å) is similar to that of Zr^{4+} (0.72 Å) and smaller than Ce^{3+} (1.01 Å; Shannon,

1976), so Ce^{4+} may substitute for Zr^{4+} in zircons. Under oxidized conditions, Ce occurs mainly as Ce^{4+} , and high Ce^{4+}/Ce^{3+} ratios thus indicate oxidized conditions:

$$Ce^{4+}/Ce^{3+} = \left(Ce_{melt} - Ce_{zircon} / D_{Ce^{3+}}^{zircon/melt} \right) / \left(Ce_{zircon} / D_{Ce^{4+}}^{zircon/melt} - Ce_{melt} \right), \quad (11)$$

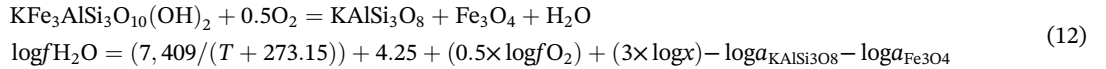
$$Ce^{4+} = \left(Ce_{melt} - Ce_{zircon} / D_{Ce^{3+}}^{zircon/melt} \right) / \left(1 / D_{Ce^{4+}}^{zircon/melt} - 1 / D_{Ce^{3+}}^{zircon/melt} \right), \quad (11.1)$$

$$Ce^{3+} = Ce_{zircon} - \left(Ce_{melt} - Ce_{zircon} / D_{Ce^{3+}}^{zircon/melt} \right) / \left(1 / D_{Ce^{4+}}^{zircon/melt} - 1 / D_{Ce^{3+}}^{zircon/melt} \right), \quad (11.2)$$

where Ce_{zircon} and Ce_{melt} represent Ce concentrations in zircon and melt and $D_{Ce^{4+}}^{zircon/melt}$ and $D_{Ce^{3+}}^{zircon/melt}$ represent partition coefficients of Ce^{4+} and Ce^{3+} between zircon and melt. The Ce^{4+}/Ce^{3+} ratio is obtained by calculating Ce^{4+} and Ce^{3+} separately using the LSM.

2.3. Biotite Oxybarometer and Thermobarometer

Biotite is commonly present in igneous rocks and reacts sensitively to changes in physicochemical conditions such as temperature, pressure, halogen fugacity, fO_2 , and magma composition (Speer, 1984). Although biotite tends to reequilibrate at subsolidus temperatures or due to hydrothermal alteration (e.g., Li et al., 2019), equilibrium assemblage biotite-magnetite-sanidine (K-feldspar) can be used to estimate magmatic fO_2 during crystallization according to the equilibrium reaction and empirical equation (Wones, 1972):



where f_{H_2O} is water fugacity, T is temperature ($^{\circ}C$), x is the mole fraction of Fe^{2+} in the octahedral site of biotite, and a is the activity of the subscripted components indicated. Waldbaum and Thompson (1969) have shown that alkali feldspar solid solutions are distinctly non-ideal. Here $a_{KAlSi_3O_8}$ is calculated from the ternary feldspar (anorthite-albite-orthoclase) model of Elkins and Grove (1990). For the calculation of f_{H_2O} , if either the partial pressure P_{H_2O} , the fugacity coefficient γ_{H_2O} , or the mole fraction in the fluid $X_{H_2O}^{fluid}$ is known, the remaining two parameters for H_2O can be solved by using the relationships:

$$P_{H_2O} = f_{H_2O} / \gamma_{H_2O} = (f_{H_2O}^{pure} \times X_{H_2O}^{fluid}) / \gamma_{H_2O}, \quad (13)$$

where $f_{H_2O}^{pure}$ is the fugacity of the pure H_2O . The γ_{H_2O} can be calculated by using the modified Redlich-Kwong equation (Holloway & Blank, 1994), given critical temperature, critical pressure, and the acentric factor ω (Iacovino, 2014; Prausnitz et al., 1998). Detailed calculation process for γ_{H_2O} can be found in the Appendix of Holloway and Blank (1994).

The solid-solution model of Woodland and Wood (1994) is used to calculate $a_{Fe_3O_4}$:

$$a_{Fe_3O_4} = (X_{mag})^2 \times \gamma_{mag}, \quad (14)$$

$$R \times T \times \ln(\gamma_{mag}) = (10,580 + 63,060 \times X_{mag}) \times (1 - X_{mag})^2, \quad (15)$$

where R is the gas constant, X_{mag} is the mole fraction of the magnetite endmember in the magnetite-ulvöspinel solid solution (Carmichael, 1966), and γ_{mag} is the activity coefficient of magnetite. X_{mag} is calculated using the similar algorithm as in the QUILF program (Andersen et al., 1993). The temperature of biotite crystallization can be obtained by the Ti-in-biotite geothermometer (see below). By substituting X_{mag} and temperature into equation (15), γ_{mag} can be calculated. Combination of equations (14) and (15) gives the value of $a_{Fe_3O_4}$.

Ti-in-biotite geothermometer is from Henry et al. (2005):

$$T (^{\circ}\text{C}) = \left(\left(\ln \text{Ti} + 2.3594 + 1.7283 \times (X_{\text{Mg}})^3 \right) / (4.6482 \times 10^{-9}) \right)^{0.333}. \quad (16)$$

This empirical equation is strictly valid only for $X_{\text{Mg}} = \text{Mg}/(\text{Mg} + \text{Fe}) = 0.275\text{--}1.000$, $\text{Ti} = 0.04\text{--}0.60$ atoms of each per formula unit calculated on the basis of 22 oxygen atoms, and $T = 480\text{--}800^{\circ}\text{C}$. Standard deviation of the Ti-in-biotite geothermometer is estimated to be $\pm 24^{\circ}\text{C}$ at temperatures of $480\text{--}600^{\circ}\text{C}$, $\pm 23^{\circ}\text{C}$ at $600\text{--}700^{\circ}\text{C}$, and $\pm 12^{\circ}\text{C}$ at $700\text{--}800^{\circ}\text{C}$ (Henry et al., 2005). Calibration of this geothermometer was based on compositions of biotite in metamorphic rocks. To check its applicability to igneous rocks, experimental data for magmatic biotites (Andújar et al., 2008; Andújar & Scaillet, 2012; Fabbrizio et al., 2006; Fabbrizio & Carroll, 2008; Mutch et al., 2016; Nandedkar et al., 2014) were used to calculate crystallization temperature using equation (16). Differences between calculated and experimentally measured temperatures were in the range of -26°C to $+65^{\circ}\text{C}$ (see supporting information Table S1). In addition, a large number of published biotite data collected from intermediate-silicic intrusions worldwide (e.g., Helmy et al., 2004; Hossain & Tsunogae, 2014; Sarjoughian et al., 2012; Wang et al., 2014) were used to check the applicability of this geothermometer in igneous systems. In the same intrusion, calculated crystallization temperatures of biotites (magmatic Mg-biotites) are 5°C to 228°C lower than crystallization temperatures of amphiboles (Mg-amphibole and Tschermakites; supporting information Table S1), which match the magmatic crystallization sequence determined by petrographic observations of each intrusion.

The pressure of magmatic biotite crystallization may be estimated using the $^{\text{T}}\text{Al}$ -geobarometer (Uchida et al., 2007):

$$P (\text{kbar}) = 3.03 \times \text{Al}_{\text{T}} - 6.53 \quad (\sigma_{\text{est}} = \pm 0.33 \text{ kbar}), \quad (17)$$

where Al_{T} is the total number of Al atoms in biotite calculated on the basis of 22 oxygens.

3. Software Description

Geo- $f\text{O}_2$ is packaged as an installation-free .exe file that can run in Windows platforms. Under Mac OS platforms, the user can also use Geo- $f\text{O}_2$ through an application such as Wine or Winebottler. Control panel interfaces consist of one main interface and three mineral subinterfaces (Figure 1). The main interface has four buttons, “Amphibole,” “Zircon,” “Biotite,” and “Quit” (Figure 1a). Clicking a mineral button brings up a corresponding mineral subinterface (Figures 1b–1d). The user is able to exit the software by clicking “Quit” or the “x” button in the upper right corner of the main interface. The mineral subinterfaces (Figures 1b–1d) are divided into two parts, which are the left OPERATION panel and right preview window showing calculated results. Main operations in the left panel include “Data input,” “Calculate,” “Save Result,” “Plot,” and “Quit.” The user can return to the main interface by clicking the “Quit” or “x” button.

3.1. Data Input

In the Data input subpanel, the user loads the data file from the desired folder. The user may view and select the input file (i.e., .csv, .xlsx, or .xls files) by clicking the “Open” button. The first column of the input file must contain the names of the oxides and/or trace elements. After selection of the input file, the program automatically extracts and rearranges data. Although this is automatic, we suggest the user uses the recommended model input Excel tables as the input files in order to avoid calculation errors caused by special characters (see supporting information tables: Table S2—model input Excel table of amphibole; Table S3—model input Excel table of zircon; Table S4—model input Excel table of host melt (or host rock) components of corresponding zircon grains used in Table S3, only one set of melt components (or bulk components) is allowed to be used per calculation; Tables S5, S6, and S7—model input Excel tables of biotite, K-feldspar, and magnetite, respectively).

3.2. Calculation

Calculation is executed by clicking the “Calculate” button in the three mineral subinterfaces (Figures 1b–1d).

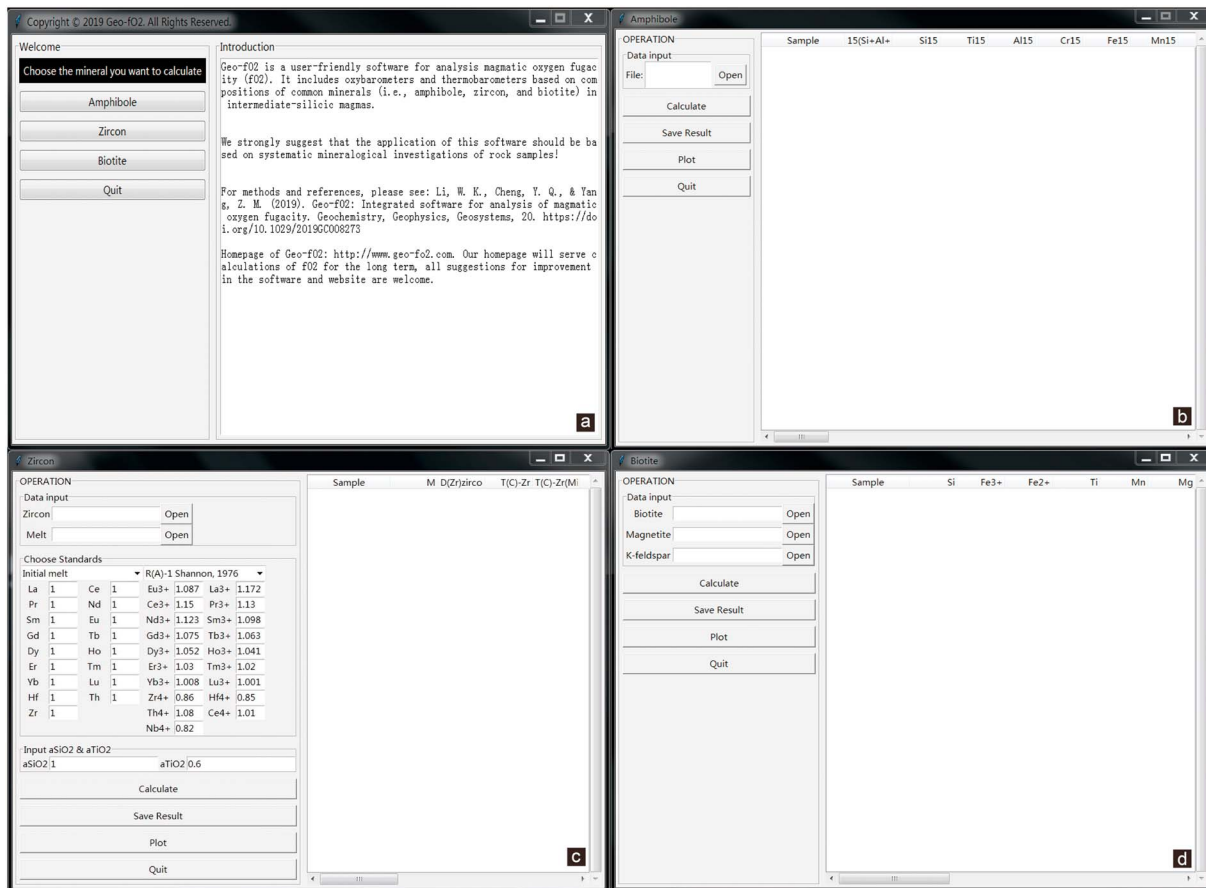


Figure 1. The main interface (a) and three mineral subinterfaces (b–d) of Geo- fO_2 illustrating major features of this software.

3.2.1. Amphibole

Calculations for amphibole use the EMPA data, with a process as shown in Figure 2. Mineral formulae for amphibole were calculated following the International Mineralogical Association recommendation for calcic amphiboles, where Fe^{3+}/Fe^{2+} ratios are determined by charge balance after adjusting total tetrahedral (Si, Al, and Ti) plus octahedral (Al, Ti, Cr, Fe, Mn, and Mg) cations to 13 (Leake et al., 1997; Ridolfi et al., 2010). Because the 13 cation calculation determines the minimum alkali content in A site (i.e., $^A(Na + K)$) and Al^{VI} , and the maximum Fe^{3+} , calculation on the basis of 15 cations is also provided to get the maximum $^A(Na + K)$ and Al^{VI} , and the minimum Fe^{3+} (Ridolfi et al., 2010). The calculated cation data are then used in amphibole classifications according to the principle of Leake et al. (1997, Figure 3 therein) and following calculations of different parameters.

Another four parallel calculations (Figure 2) based on calculated amphibole cation data include P , T , ΔNNO value, and H_2O content. Calculations of Si^* -sensitive thermometer and $\Delta NNO-Mg^*$ oxybarometer are very stable within the conditions of 550–1120 °C and $-1 \leq \Delta NNO \leq +5$ (Ridolfi et al., 2010). The calculated ΔNNO is converted into ΔFMQ and ΔHM values (ΔFMQ and ΔHM are the deviation of $\log fO_2$ from the fayalite-magnetite-quartz buffer [FMQ; O'Neill, 1987] and the hematite-magnetite buffer [HM; Nasir, 1994]), based on two sets of combined values of calculated temperatures and pressures (Figure 2). The program also translates ΔNNO into absolute $\log fO_2$. Although calculated standard error of Al_T -sensitive barometer is 0.54 kbar, it strongly decreases to 0.39 kbar at $P < 4.5$ kbar, where the average relative error is $\pm 14\%$ (Ridolfi et al., 2010). At 1 GPa, the relative error can be as high as 33%, but it decreases to 8% for the amphiboles at the physical-chemical stability boundaries (Ridolfi et al., 2010). The relative error of this barometer is $< 11\%$ near the P - T stability curve, whereas for crystal-rich (i.e., porphyritic index $> 35\%$) and lower- T magmas, the relative error increases up to 24%, consistent with depth relative error of ± 0.4 km at

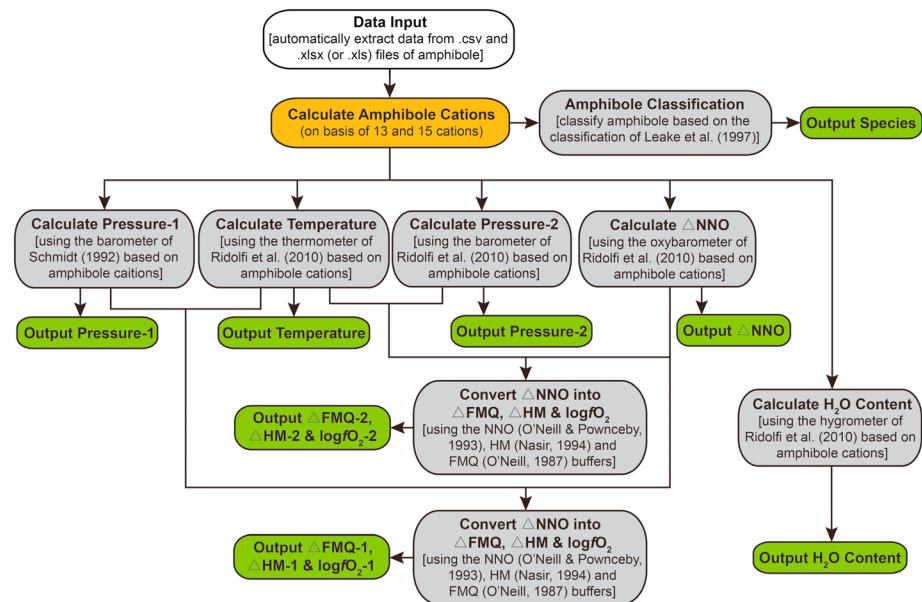


Figure 2. Flowcharts summarizing the basic workflow for calculating mineral cations and thermodynamic parameters on the basis of amphibole. White box represents data input and extract process; orange box represents mineral cations calculation process based on mineral formulae; gray boxes are the calculation process of T , P , and fO_2 ; green boxes represent the output process of calculated T , P , and fO_2 data. NNO = Ni–NiO buffer; FMQ = fayalite-magnetite-quartz buffer; HM = hematite-magnetite buffer.

0.9 kbar (~3.4 km) and ± 7.9 km at 8.0 kbar (~30 km). As a result, we strongly suggest using this barometer with amphibole compositions having $Al^V/Al_T \leq 0.21$ and $Mg/(Mg + Fe^{2+}) > 0.5$ (Ridolfi et al., 2010). The user may preview all results in the right preview window for each mineral subinterface (Figures 1b–1d).

3.2.2. Zircon

Zircon calculations are based on elemental contents of zircon (i.e., trace element) and host rock (i.e., major and trace elements). Calculation processes are shown in Figure 3. By default, Geo- fO_2 only allows the user to calculate zircon data from one rock sample at one time because Geo- fO_2 has no automatic matching function. For example, if the user has two groups of zircon trace element data from two different rock samples, Samples 1 and 2, fO_2 values of the two groups should be calculated separately, using the corresponding combination of zircons and host rock. More specifically, by inputting bulk components of Sample 1 and trace element data of zircons yielded in rock Sample 1, the user can obtain fO_2 values of Sample 1. If the user wants to get fO_2 values of Sample 2, the user has to repeat above calculation procedure. In this case, the user therefore cannot get two groups of fO_2 values through one calculation.

The Zr saturation temperature is calculated from the partitioning of Zr between zircon and host melt. The program gives two sets of Zr saturation temperature based on two thermometers (Miller et al., 2003; Watson & Harrison, 1983). Before calculation of temperature by the Ti-in-zircon thermometer, the program requires the user to manually set a_{SiO_2} and a_{TiO_2} values through input boxes in the “Input a_{SiO_2} & a_{TiO_2} ” subpanel (Figure 1c). The initial values are set to 1.0 and 0.6, respectively (0.6 is almost the minimum in silicic melts; Ferry & Watson, 2007; Hayden & Watson, 2007; Watson et al., 2006). Therefore, three temperatures (two Zr saturation and one Ti-in-zircon temperatures) are provided in the final output Excel table based on one set of zircon-melt data (Figure 3).

The zircon subinterface has an extra subpanel, “Choose Standards,” which serves the $(Ce/Ce^*)_D$ calculation. When the input file of melt components is selected, the program automatically extracts REE, Hf, Th, and Zr data and lists them in corresponding boxes for “Initial melt” in the first dropdown box (Figure 1c). The user may also choose alternative normalized standards provided in the dropdown box, for example, C1, E-MORB, N-MORB, and OIB standards of Sun and McDonough (1989) and upper, lower, and bulk continental crust and oceanic crust standards of Taylor and McLennan (1985), to calculate $(Ce/Ce^*)_D$ values. Ce^{4+}/Ce^{3+}

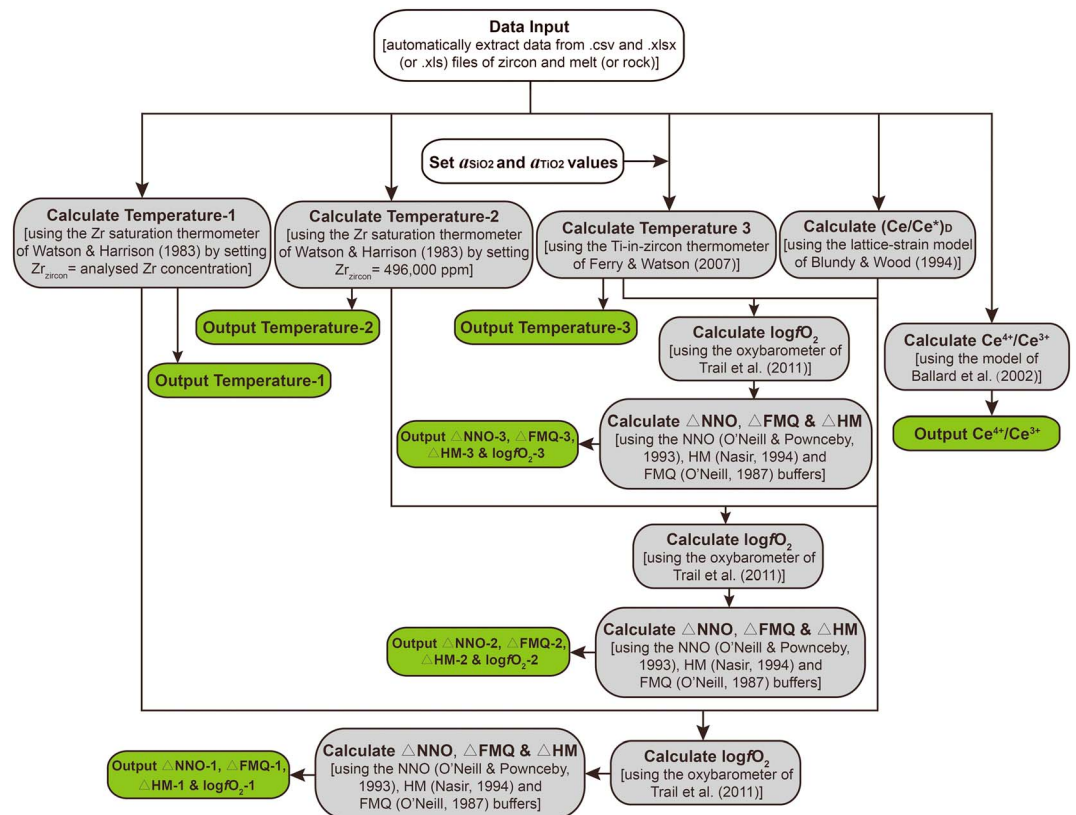


Figure 3. Flowcharts summarizing the basic workflow for calculating thermodynamic parameters on the basis of the composition of zircon and its host melt (or rock). Meanings of different colored boxes are as in Figure 2. NNO = Ni-NiO buffer; FMQ = fayalite-magnetite-quartz buffer; HM = hematite-magnetite buffer.

ratios are synchronously calculated with $(\text{Ce}/\text{Ce}^*)_{\text{D}}$ values through similar processes. The second dropdown box in the “Choose Standards” subpanel provides two similar sets of radii data (Shannon, 1976), namely, the “R(A)-1” (crystal radius) and “R(A)-2” (effective ionic radius), for use in calculating $(r_i/3 + r_o/6) \times (r_i - r_o)^2$ for the $(\text{Ce}/\text{Ce}^*)_{\text{D}}$ calculation (equation (8)). The user may also enter other numbers in the input boxes, from which the program will calculate new $(\text{Ce}/\text{Ce}^*)_{\text{D}}$ values. Finally, $f\text{O}_2$ is calculated on the basis of temperature and $(\text{Ce}/\text{Ce}^*)_{\text{D}}$ (Figure 3).

3.2.3. Biotite

Calculations for biotite are based on EMPA data for biotite, K-feldspar, and magnetite. Again, the first step converts oxides to cations on the basis of mineral formulae. Cation data are then used in calculations as shown in Figure 4.

Then three parallel calculations are performed using cation composition of biotite, for x value, P , and T (Figure 4). The user can run multiple biotite, magnetite, and K-feldspar at the same time, and they will not be cross-correlated. However, the three minerals must all be from the same rock. Calculated T and P results by biotite compositions will be averaged and combined in the subsequent calculation of $a_{\text{KAlSi}_3\text{O}_8}$ values with cation components of K-feldspar (Figure 4). Meanwhile, $a_{\text{Fe}_3\text{O}_4}$ values are calculated using average T and cation components of magnetite, and $f\text{H}_2\text{O}$ is calculated using equation (13) with calculated individual temperature and pressure based on each biotite composition (Figure 4). Finally, $f\text{H}_2\text{O}$, $a_{\text{KAlSi}_3\text{O}_8}$, and $a_{\text{Fe}_3\text{O}_4}$ will be averaged and used to calculate $f\text{O}_2$ with x value and T by using equation (12) (Figure 4).

3.3. Data Output

To save calculated results, the user clicks the “Save Result” button for each mineral subinterface (Figures 1b–1d) and selects the desired folder. The program creates Excel tables (.xlsx files) as default saved files.

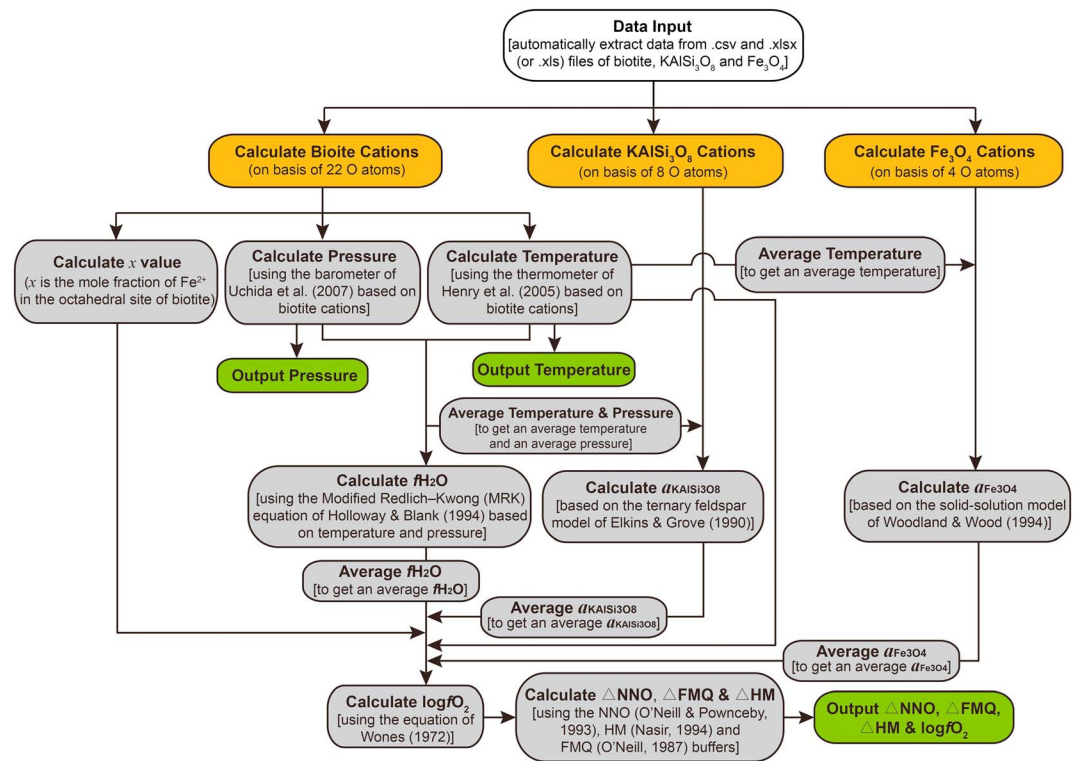


Figure 4. Flowcharts summarizing the basic workflow for calculating mineral cations and thermodynamic parameters on the basis of biotite, K-feldspar, and magnetite. Note that the used temperature values in the last step of $\log fO_2$ calculation are the calculated individual temperature based on each biotite composition. Meanings of different colored boxes are as in Figure 2. NNO = Ni–NiO buffer; FMQ = fayalite-magnetite-quartz buffer; HM = hematite-magnetite buffer.

3.4. Plotting

The user may enter the plotting interface via the “Plot” button (Figure 1). Plotting and graphic capabilities of the program are based on Matplotlib modules (Hunter, 2007). As an example, the plotting interface for amphibole is divided into a left “Operation” panel and right plot window (Figure 5). The user selects X and Y coordinate axes from the dropdown menu in left “Operation” panel, with these axes sharing the same options, including calculated mineral compositions and thermodynamic parameters (T , P , and fO_2). The user can respectively rename X and Y axes through manual input boxes (i.e., “X Axes” and “Y Axes”) under dropdown menu boxes of X and Y (Figure 5), though the initial name of X and Y axes in the rename box is set to the same as that selected in the dropdown menu. Axes ranges are set in the “X Limits” and “Y Limits” boxes (Figure 5). A figure title can be entered in the “Title” box, with linear or logarithmic scales set in the “Scales” box (Figure 5). Symbols of different color and shape can be selected via the “Color” and “Shape” dropdown menu boxes (Figure 5). After the user chooses linear or logarithmic scale, the program will automatically judge which axes can be converted to linear or logarithmic scale. Note that the logarithmic scale does not apply to all chosen axes. For instance, the calculated $\log fO_2$ value is often less than 0, the logarithmic scale for such a negative $\log fO_2$ axis does not work and no data will be shown in the right plot window.

Once axes and symbols are set, the user clicks the “Plot” button to plot data on the binary diagram in the right plot window (Figure 5). Axes and symbols can be adjusted in the left panel before saving the image. However, contents of boxes in left “Operation” panel may be modified many times by the user, clicking the “Plot” button displays each modified contents in plot window. The “Save Image” button allows saving of the image in the Scalable Vector Graphics (SVG) format. The SVG image may be edited in Adobe Illustrator, Adobe Photoshop, CorelDRAW, or other image-processing software. The commonly used model diagrams are provided in the supporting information diagram file so that the user can use these when modifying saved SVG images.

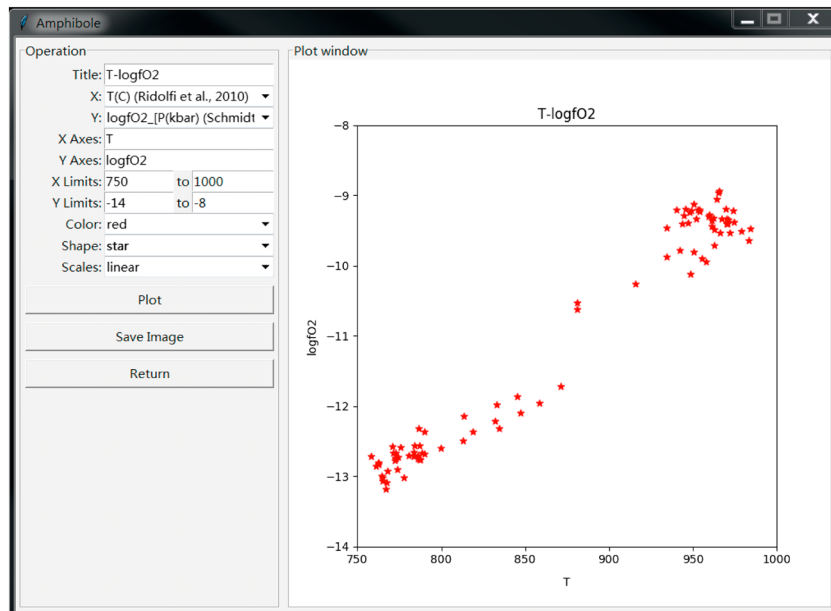


Figure 5. Plotting subinterface of amphibole showing the procedure to plot the binary diagrams. Data source is Table S8.

4. Calculation Examples

4.1. Amphibole

Take the 91 given amphibole data from Jiru, Qulong, and Jiama deposits in Tibet (Table S8; Wang et al., 2014) as an example, the user can copy them from Table S8 and paste them into the model input Excel Table S2 of amphibole and save data. Through the subinterface of amphibole (Figure 1b), the user loads filled Table S2 and calculates various parameters by clicking the “Calculate” button.

Amphibole of Tibetan samples comprises Tschermakite, Mg-hastingsite and Mg-amphibole. The calculated temperatures and H₂O contents for amphiboles are 758–984 °C and 2.9–6.5 wt.%, respectively (Table S8). Pressure values calculated by equation (3) range from 0.7 to 5.3 kbar (corresponding to a continental depth of 2–20 km), while values calculated by equation (5) range from 1.1 to 8.0 kbar (corresponding to a continental depth of 4–30 km). Based on the two pressure values, Geo-*f*O₂ will provide two sets of *f*O₂ value (Δ FMQ), respectively, +0.8 to +2.7, and +1.0 to +2.8 (Table S8).

4.2. Zircon

Trace element data and calculated results of zircon from Jiru (JR) and Xueba (XB) area in Tibet (Wang et al., 2014) are provided in Table S9. Table S9 also contains three corresponding bulk component data of JR-2, JR11-06, and XB-12. As mentioned above, Geo-*f*O₂ has no automatic matching function, so the user needs to calculate *f*O₂ values of JR-2, JR11-06, and XB-12 separately. For example, the user can copy bulk component data of JR-2 and three trace element data of zircons (i.e., JR-2_3, JR-2_4, and JR-2_5) yielded in rock JR-2 from Table S9 then respectively paste them into the model input Excel Tables S4 and S3 and save data. By inputting Tables S4 and S3 through the zircon subinterface, the user can obtain Ce⁴⁺/Ce³⁺ ratio (82–119; Table S9), temperature, and *f*O₂ values of JR-2. As Geo-*f*O₂ contains three thermometers of zircon (Ferry & Watson, 2007; Miller et al., 2003; Watson & Harrison, 1983), three sets of *f*O₂ values (i.e., Δ FMQ = +3.73 to +5.13; +3.69 to +5.09; +3.07 to +4.67; Table S9) therefore will be calculated respectively based on three temperature results (i.e., 734–735 °C; 733 °C; 708–740 °C; Table S9). Then calculated temperature and *f*O₂ values will be saved in output file by clicking the “Save Result” button in zircon subinterface (Figure 1c). Through repeating above calculation procedure, the user can respectively get Ce⁴⁺/Ce³⁺ ratio, temperature, and *f*O₂ values of sample JR11-06 and XB12-3 (see results in Table S9). In order to avoid error caused by incorrect operation, only column B in Table S4 is allowed to input the only one set of bulk component data at one time, while other columns are locked.

4.3. Biotite

Table S10 contains EMPA data and calculated results of biotite, K-feldspar, and magnetite from the Pulang deposit (Li et al., 2019). Each example of each mineral are from the same rock sample (i.e., 15PL-04; Li et al., 2019).

As calculation in biotite section does not require cross correlation among data of three minerals, the user can paste the six given EMPA data (Table S10) of biotite into model input Excel Table S5, the five given EMPA data of K-feldspar into Table S6, and the three given EMPA data of magnetite into Table S7 and save data in each table. After input Tables S5, S6, and S7 in biotite subinterface (Figure 1d), the user can get the crystallization temperature and pressure of biotite ($T = 731\text{--}748\text{ }^{\circ}\text{C}$; $P = 0.9\text{--}1.1\text{ kbar}$; Table S10). The average temperature and pressure ($741\text{ }^{\circ}\text{C}$ and 1.0 kbar) will be joined into the calculation of $f\text{H}_2\text{O}$, $\alpha_{\text{KAlSi}_3\text{O}_8}$, and $\alpha_{\text{Fe}_3\text{O}_4}$. Finally, the $f\text{O}_2$ values ($\Delta\text{FMQ} = +1.1\text{ to }+1.5$; Table S10) will be calculated through equation (12).

5. Summary

Geo- $f\text{O}_2$ is specialized software for calculating and visualizing magmatic $f\text{O}_2$ based on oxybarometers and thermobarometers for amphibole, zircon, and biotite in intermediate-silicic magmas. It runs in Windows platforms and requires no installation. It automatically extracts data from Excel tables or .csv files, with calculated results being displayed in Excel tables. With user-friendly interfaces, it is able to plot data on many different binary diagrams, which may be saved in SVG format.

Acknowledgments

This work was funded by the National Key Research and Development Project of China (2016YFC0600305) and the National Natural Science Foundation of China (41825005, 41273051, and 41473041). We thank Fuat Yavuz, Filippo Ridolfi, Rui Wang, and Junting Qiu for guidance of calculation and Yulei Zhao for design of cover icon. Suzanne K. Birner and an anonymous reviewer are thanked for their thorough and constructive reviews. We appreciate Editor Janne Blichert-Toft and an anonymous Associate Editor of *Geochemistry, Geophysics, Geosystems* for their constructive comments and editing. Geo- $f\text{O}_2$ is encouraged to be downloaded from our homepage (<http://geo-fo2.com>), on which the latest version of the software will be available. Our homepage will also serve calculations of $f\text{O}_2$ for the long term; all suggestions for improvement in the software and website are welcome. Model input Excel tables, examples, and model diagrams are provided in the supporting information.

References

- Allen, J. C., & Boettcher, A. L. (1978). Amphiboles in andesite and basalt: II. Stability as a function of P-T- $f\text{H}_2\text{O}$ - $f\text{O}_2$. *American Mineralogist*, 63(11-12), 1074-1087.
- Andersen, D. J., & Lindsley, D. H. (1985). New (and final!) models for the Ti-magnetite/ilmenite geothermometer and oxygen barometer. Abstract AGU 1985 Spring Meeting Eos Transactions. American Geophysical Union 66 (18), 416.
- Andersen, D. J., Lindsley, D. H., & Davidson, P. M. (1993). QUILF: A pascal program to assess equilibria among Fe-Mn-Ti oxides, pyroxenes, olivine, and quartz. *Computers & Geosciences*, 19(9), 1333-1350. [https://doi.org/10.1016/0098-3004\(93\)90033-2](https://doi.org/10.1016/0098-3004(93)90033-2)
- Andújar, J., Costa, F., Martí, J., Wolff, J. A., & Carroll, M. R. (2008). Experimental constraints on pre-eruptive conditions of phonolitic magma from the caldera-forming El Abrigo eruption, Tenerife (Canary Islands). *Chemical Geology*, 257(3-4), 173-191. <https://doi.org/10.1016/j.chemgeo.2008.08.012>
- Andújar, J., & Scaillet, B. (2012). Experimental constraints on parameters controlling the difference in the eruptive dynamics of phonolitic magmas: The case of Tenerife (Canary Islands). *Journal of Petrology*, 53(9), 1777-1806. <https://doi.org/10.1093/petrology/egs033>
- Ballard, J. R., Palin, M. J., & Campbell, I. H. (2002). Relative oxidation states of magmas inferred from Ce (IV)/Ce (III) in zircon: Application to porphyry copper deposits of northern Chile. *Contributions to Mineralogy and Petrology*, 144(3), 347-364. <https://doi.org/10.1007/s00410-002-0402-5>
- Blundy, J., & Wood, B. (1994). Prediction of crystal-melt partition coefficients from elastic moduli. *Nature*, 372, 452-454. <https://doi.org/10.1038/372452a0>
- Brounce, M. N., Kelley, K. A., & Cottrell, E. (2014). Variations in $\text{Fe}^{3+}/\Sigma\text{Fe}$ of Mariana Arc basalts and mantle wedge $f\text{O}_2$. *Journal of Petrology*, 55(12), 2513-2536. <https://doi.org/10.1093/petrology/egu065>
- Buddington, A. F., & Lindsley, D. H. (1964). Iron-titanium oxide minerals and synthetic equivalents. *Journal of Petrology*, 5(2), 310-357. <https://doi.org/10.1093/petrology/5.2.310>
- Burgisser, A., & Scaillet, B. (2007). Redox evolution of a degassing magma rising to the surface. *Nature*, 445(7124), 194. <https://doi.org/10.1038/nature05509>
- Burnham, A. D., & Berry, A. J. (2012). An experimental study of trace element partitioning between zircon and melt as a function of oxygen fugacity. *Geochimica et Cosmochimica Acta*, 95, 196-212. <https://doi.org/10.1016/j.gca.2012.07.034>
- Canil, D. (2002). Vanadium in peridotites, mantle redox and tectonic environments: Archean to present. *Earth and Planetary Science Letters*, 195(1-2), 75-90. [https://doi.org/10.1016/S0012-821X\(01\)00582-9](https://doi.org/10.1016/S0012-821X(01)00582-9)
- Carmichael, I. S. E. (1966). The iron-titanium oxides of salic volcanic rocks and their associated ferromagnesian silicates. *Contributions to Mineralogy and Petrology*, 14(1), 36-64. <https://doi.org/10.1007/BF00370985>
- Carmichael, I. S. E. (1991). The redox states of basic and silicic magmas: A reflection of their source regions? *Contributions to Mineralogy and Petrology*, 106, 129-141. <https://doi.org/10.1007/BF00306429>
- Cherniak, D. J., Hanchar, J. M., & Watson, E. B. (1997). Rare-earth diffusion in zircon. *Chemical Geology*, 134(4), 289-301. [https://doi.org/10.1016/S0009-2541\(96\)00098-8](https://doi.org/10.1016/S0009-2541(96)00098-8)
- Clémente, B., Scaillet, B., & Pichavant, M. (2004). The solubility of sulphur in hydrous rhyolitic melts. *Journal of Petrology*, 45(11), 2171-2196. <https://doi.org/10.1093/petrology/egh052>
- Cottrell, E., & Kelley, K. A. (2011). The oxidation state of Fe in MORB glasses and the oxygen fugacity of the upper mantle. *Earth and Planetary Science Letters*, 305(3), 270-282. <https://doi.org/10.1016/j.epsl.2011.03.014>
- Danyushevsky, L. V., & Plechov, P. (2011). Petrolog3: Integrated software for modeling crystallization processes. *Geochemistry, Geophysics, Geosystems*, 12, Q07021. <https://doi.org/10.1029/2011GC003516>
- Dilles, J. H., Kent, A. J., Wooden, J. L., Tosdal, R. M., Koleszar, A., Lee, R. G., & Farmer, L. P. (2015). Zircon compositional evidence for sulfur-degassing from ore-forming arc magmas. *Economic Geology*, 110(1), 241-251. <https://doi.org/10.2113/econgeo.110.1.241>
- Eggler, D. H. (1972). Amphibole stability in H_2O -undersaturated calc-alkaline melts. *Earth and Planetary Science Letters*, 15(1), 28-34. [https://doi.org/10.1016/0012-821X\(72\)90025-8](https://doi.org/10.1016/0012-821X(72)90025-8)

- Elderfield, H., Hawkesworth, C. J., Greaves, M. J., & Calvert, S. E. (1981). Rare earth element zonation in Pacific ferromanganese nodules. *Geochimica et Cosmochimica Acta*, 45(7), 1231–1234. [https://doi.org/10.1016/0016-7037\(81\)90146-0](https://doi.org/10.1016/0016-7037(81)90146-0)
- Elkins, L. T., & Grove, T. L. (1990). Ternary feldspar experiments and thermodynamic models. *American Mineralogist*, 75(5–6), 544–559.
- Evans, K. A., & Tomkins, A. G. (2011). The relationship between subduction zone redox budget and arc magma fertility. *Earth and Planetary Science Letters*, 308(3–4), 401–409. <https://doi.org/10.1016/j.epsl.2011.06.009>
- Fabbrizio, A., & Carroll, M. R. (2008). Experimental constraints on the differentiation process and pre-eruptive conditions in the magmatic system of phlegraean fields (Naples, Italy). *Journal of Volcanology and Geothermal Research*, 171(1), 88–102. <https://doi.org/10.1016/j.jvolgeores.2007.11.002>
- Fabbrizio, E., Rouse, P. J., & Carroll, M. R. (2006). New experimental data on biotite+magnetite+sanidine saturated phonolitic melts and application to the estimation of magmatic water fugacity. *American Mineralogist*, 91(11–12), 1863–1870. <https://doi.org/10.2138/am.2006.2055>
- Ferry, J. M., & Watson, E. B. (2007). New thermodynamic models and revised calibrations for the Ti-in-zircon and Zr-in-rutile thermometers. *Contributions to Mineralogy and Petrology*, 154(4), 429–437. <https://doi.org/10.1007/s00410-007-0201-0>
- Frost, B. R. (1991). Introduction to oxygen fugacity and its petrologic importance. In D. H. Lindsley (Ed.), *Oxide Minerals: Petrologic and Magnetic Significance. Reviews in Mineralogy* (Vol. 25, pp. 1–9). Washington, DC: Mineral. Soc. Am.
- Ghiorso, M. S., & Gualda, G. A. (2013). A method for estimating the activity of titania in magmatic liquids from the compositions of coexisting rhombohedral and cubic iron–titanium oxides. *Contributions to Mineralogy and Petrology*, 165(1), 73–81. <https://doi.org/10.1007/s00410-012-0792-y>
- Ghiorso, M. S., Hirschmann, M. M., Reiners, P. W., & Kress, V. C. III (2002). The pMELTS: A revision of MELTS for improved calculation of phase relations and major element partitioning related to partial melting of the mantle to 3 GPa. *Geochemistry, Geophysics, Geosystems*, 3(5), 1030. <https://doi.org/10.1029/2001GC000217>
- Ghiorso, M. S., & Sack, O. (1991). Fe-Ti oxide geothermometry: Thermodynamic formulation and the estimation of intensive variables in silicic magmas. *Contributions to Mineralogy and Petrology*, 108(4), 485–510. <https://doi.org/10.1007/BF00303452>
- Ghiorso, M. S., & Sack, R. O. (1995). Chemical mass transfer in magmatic processes IV. A revised and internally consistent thermodynamic model for the interpolation and extrapolation of liquid–solid equilibria in magmatic systems at elevated temperatures and pressures. *Contributions to Mineralogy and Petrology*, 119(2–3), 197–212. <https://doi.org/10.1007/BF00307281>
- Hayden, L. A., & Watson, E. B. (2007). Rutile saturation in hydrous siliceous melts and its bearing on Ti-thermometry of quartz and zircon. *Earth and Planetary Science Letters*, 258(3–4), 561–568. <https://doi.org/10.1016/j.epsl.2007.04.020>
- Helmy, H. M., Ahmed, A. F., El Mahallawi, M. M., & Ali, S. M. (2004). Pressure, temperature and oxygen fugacity conditions of calc-alkaline granitoids, Eastern Desert of Egypt, and tectonic implications. *Journal of African Earth Sciences*, 38(3), 255–268. <https://doi.org/10.1016/j.jafrearsci.2004.01.002>
- Henry, D. J., Guidotti, C. V., & Thomson, J. A. (2005). The Ti-saturation surface for low-to-medium pressure metapelitic biotites: Implications for geothermometry and Ti-substitution mechanisms. *American Mineralogist*, 90(2–3), 316–328. <https://doi.org/10.2138/am.2005.1498>
- Hinton, R. W., & Upton, B. G. J. (1991). The chemistry of zircon: Variations within and between large crystals from syenite and alkali basalt xenoliths. *Geochimica et Cosmochimica Acta*, 55(11), 3287–3302. [https://doi.org/10.1016/0016-7037\(91\)90489-R](https://doi.org/10.1016/0016-7037(91)90489-R)
- Holloway, J. R., & Blank, J. G. (1994). Application of experimental results to C-O-H species in natural melts. *Reviews in Mineralogy and Geochemistry*, 30(1), 187–230.
- Hossain, I., & Tsunogae, T. (2014). Crystallization conditions and petrogenesis of the paleoproterozoic basement rocks in Bangladesh: An evaluation of biotite and coexisting amphibole mineral chemistry. *Journal of Earth Science*, 25(1), 87–97. <https://doi.org/10.1007/s12583-014-0402-1>
- Hunter, J. D. (2007). Matplotlib: A 2D graphics environment. *Computing in Science & Engineering*, 9(3), 90–95. <https://doi.org/10.1109/MCSE.2007.55>
- Iacono-Marziano, G., Gaillard, F., Scaillet, B., Polozov, A. G., Marechal, V., Pirre, M., & Arndt, N. T. (2012). Extremely reducing conditions reached during basaltic intrusion in organic matter-bearing sediments. *Earth and Planetary Science Letters*, 357, 319–326. <https://doi.org/10.1016/j.epsl.2012.09.052>
- Iacovino, K. (2014). An unexpected journey: Experimental insights into magma and volatile transport beneath Erebus volcano, Antarctica (Doctoral dissertation, University of Cambridge). <https://doi.org/10.17863/CAM.16442>
- Jugo, P. J. (2009). Sulfur content at sulfide saturation in oxidized magmas. *Geology*, 37(5), 415–418. <https://doi.org/10.1130/G25527A.1>
- Jugo, P. J., Luth, R. W., & Richards, J. P. (2005). Experimental data on the speciation of sulfur as a function of oxygen fugacity in basaltic melts. *Geochimica et Cosmochimica Acta*, 69(2), 497–503. <https://doi.org/10.1016/j.gca.2004.07.011>
- Kennedy, G. C. (1948). Equilibrium between volatiles and iron oxides in igneous rocks. *American Journal of Science*, 246(9), 529–548.
- Kilinc, A., Carmichael, I. S. E., Rivers, M. L., & Sack, R. O. (1983). The ferric-ferrous ratio of natural silicate liquids equilibrated in air. *Contributions to Mineralogy and Petrology*, 83(1–2), 136–140. <https://doi.org/10.1007/BF00373086>
- Kress, V. C., & Carmichael, I. S. (1991). The compressibility of silicate liquids containing Fe₂O₃ and the effect of composition, temperature, oxygen fugacity and pressure on their redox states. *Contributions to Mineralogy and Petrology*, 108(1–2), 82–92. <https://doi.org/10.1007/BF00307328>
- Leake, B. E., Woolley, A. R., Arps, C. E. S., Birch, W. D., Gilbert, M. C., Grice, J. D., et al. (1997). Nomenclature of amphiboles: Report of the subcommittee on amphiboles of the International Mineralogical Association Commission on New Minerals and Mineral Names. *The Canadian Mineralogist*, 61(405), 295–310. <https://doi.org/10.1180/minmag.1997.061.405.13>
- Lee, C. T. A., Leeman, W. P., Canil, D., & Li, Z. X. A. (2005). Similar V/Sc systematics in MORB and arc basalts: Implications for the oxygen fugacities of their mantle source regions. *Journal of Petrology*, 46(11), 2313–2336. <https://doi.org/10.1093/petrology/egi056>
- Lepage, L. D. (2003). ILMAT: An excel worksheet for ilmenite–magnetite geothermometry and geobarometry. *Computers & Geosciences*, 29(5), 673–678. [https://doi.org/10.1016/S0098-3004\(03\)00042-6](https://doi.org/10.1016/S0098-3004(03)00042-6)
- Li, W. K., Yang, Z. M., Cao, K., Lu, Y. J., & Sun, M. Y. (2019). Redox-controlled generation of the giant porphyry Cu–Au deposit at Pulang, southwest China. *Contributions to Mineralogy and Petrology*, 174(2), 12. <https://doi.org/10.1007/s00410-019-1546-x>
- Mathez, E. A. (1984). Influence of degassing on oxidation states of basaltic magmas. *Nature*, 310(5976), 371. <https://doi.org/10.1038/310371a0>
- Miller, C. F., McDowell, S. M., & Mapes, R. W. (2003). Hot and cold granites? Implications of zircon saturation temperatures and preservation of inheritance. *Geology*, 31(6), 529–532. [https://doi.org/10.1130/0091-7613\(2003\)031<0529:HACGIO>2.0.CO;2](https://doi.org/10.1130/0091-7613(2003)031<0529:HACGIO>2.0.CO;2)
- Moretti, R., & Ottonello, G. (2005). Solubility and speciation of sulfur in silicate melts: The Conjugated Toop-Samis-Flood-Grjotheim (CTSFG) model. *Geochimica et Cosmochimica Acta*, 69(4), 801–823. <https://doi.org/10.1016/j.gca.2004.09.006>

- Mutch, E. J. F., Blundy, J. D., Tattitch, B. C., Cooper, F. J., & Brooker, R. A. (2016). An experimental study of amphibole stability in low-pressure granitic magmas and a revised Al-in-hornblende geobarometer. *Contributions to Mineralogy and Petrology*, 171(10), 85. <https://doi.org/10.1007/s00410-016-1298-9>
- Nandedkar, R. H., Ulmer, P., & Müntener, O. (2014). Fractional crystallization of primitive, hydrous arc magmas: An experimental study at 0.7 GPa. *Contributions to Mineralogy and Petrology*, 167(6), 1015. <https://doi.org/10.1007/s00410-014-1015-5>
- Nasir, S. (1994). PTOXY: Software package for the calculation of pressure-temperature-oxygen fugacity using a selection of metamorphic geothermobarometers. *Computers and Geosciences*, 20(9), 1297–1320. [https://doi.org/10.1016/0098-3004\(94\)90056-6](https://doi.org/10.1016/0098-3004(94)90056-6)
- O'Neill, H. S. (1987). Quartz-fayalite-iron and quartz-fayalite-magnetite equilibria and the free energy of formation of fayalite (Fe₂SiO₄) and magnetite (Fe₃O₄). *American Mineralogist*, 72(1-2), 67–75.
- O'Neill, H. S., & Pownceby, M. I. (1993). Thermodynamic data from redox reactions at high temperatures. I. An experimental and theoretical assessment of the electrochemical method using stabilized zirconia electrolytes, with revised values for the Fe–“FeO”, Co–CoO, Ni–NiO, and Cu–Cu₂O oxygen buffers, and new data for the W–WO₂ buffer. *Contributions to Mineralogy and Petrology*, 114, 296–314. <https://doi.org/10.1007/BF01046533>
- Pawley, A. R., Holloway, J. R., & McMillan, P. F. (1992). The effect of oxygen fugacity on the solubility of carbon-oxygen fluids in basaltic melt. *Earth and Planetary Science Letters*, 110, 213–225. [https://doi.org/10.1016/0012-821X\(92\)90049-2](https://doi.org/10.1016/0012-821X(92)90049-2)
- Prausnitz, J. M., Lichtenthaler, R. N., & de Azevedo, E. G. (1998). Molecular thermodynamics of fluid-phase equilibria. Pearson Education.
- Qiu, J. T., Yu, X. Q., Santosh, M., Zhang, D. H., Chen, S. Q., & Li, P. J. (2013). Geochronology and magmatic oxygen fugacity of the Tongcun molybdenum deposit, northwest Zhejiang, SE China. *Mineralium Deposita*, 48(5), 545–556. <https://doi.org/10.1007/s00126-013-0456-5>
- Richards, J. P. (2015). The oxidation state, and sulfur and Cu contents of arc magmas: implications for metallogeny. *Lithos*, 233, 27–45. <https://doi.org/10.1016/j.lithos.2014.12.011>
- Ridolfi, F., & Renzulli, A. (2012). Calcic amphiboles in calc-alkaline and alkaline magmas: Thermobarometric and chemometric empirical equations valid up to 1,130°C and 2.2 GPa. *Contributions to Mineralogy and Petrology*, 163(5), 877–895. <https://doi.org/10.1007/s00410-011-0704-6>
- Ridolfi, F., Renzulli, A., & Puerini, M. (2010). Stability and chemical equilibrium of amphibole in calc-alkaline magmas: An overview, new thermobarometric formulations and application to subduction-related volcanoes. *Contributions to Mineralogy and Petrology*, 160(1), 45–66. <https://doi.org/10.1007/s00410-009-0465-7>
- Rowe, M. C., Kent, A. J., & Nielsen, R. L. (2009). Subduction influence on oxygen fugacity and trace and volatile elements in basalts across the Cascade Volcanic Arc. *Journal of Petrology*, 50(1), 61–91. <https://doi.org/10.1093/petrology/egn072>
- Sack, R. O., Carmichael, I. S. E., Rivers, M. L., & Ghiorso, M. S. (1981). Ferric-ferrous equilibria in natural silicate liquids at 1 bar. *Contributions to Mineralogy and Petrology*, 75(4), 369–376. <https://doi.org/10.1007/BF00374720>
- Sano, Y., Terada, K., & Fukuoka, T. (2002). High mass resolution ion microprobe analysis of rare earth elements in silicate glass, apatite and zircon: Lack of matrix dependency. *Chemical Geology*, 184(3), 217–230. [https://doi.org/10.1016/S0009-2541\(01\)00366-7](https://doi.org/10.1016/S0009-2541(01)00366-7)
- Sarjoughian, F., Kananian, A., Haschke, M., Ahmadian, J., Ling, W., & Zong, K. (2012). Magma mingling and hybridization in the Kuh-e Dom pluton, Central Iran. *Journal of Asian Earth Sciences*, 54, 49–63. <https://doi.org/10.1016/j.jseae.2012.03.013>
- Schmidt, M. W. (1992). Amphibole composition in tonalite as a function of pressure; an experimental calibration of the Al-in-hornblende barometer. *Contributions to Mineralogy and Petrology*, 110, 304–310. <https://doi.org/10.1007/BF00310745>
- Shannon, R. T. (1976). Revised effective ionic radii and systematic studies of interatomic distances in halides and chalcogenides. *Acta Crystallographica, Section A: Crystal Physics, Diffraction, Theoretical and General Crystallography*, 32(5), 751–767. <https://doi.org/10.1107/S0567739476001551>
- Sillitoe, R. H. (2010). Porphyry copper systems. *Economic Geology*, 105(1), 3–41. <https://doi.org/10.2113/gsecongeo.105.1.3>
- Simon, A. C., & Ripley, E. M. (2011). The role of magmatic sulfur in the formation of ore deposits. *Reviews in Mineralogy and Geochemistry*, 73(1), 513–578. <https://doi.org/10.2138/rmg.2011.73.16>
- Skora, S., & Blundy, J. (2010). High-pressure hydrous phase relations of radiolarian clay and implications for the involvement of subducted sediment in arc magmatism. *Journal of Petrology*, 51(11), 2211–2243. <https://doi.org/10.1093/petrology/egq054>
- Smith, P. M., & Asimow, P. D. (2005). Adiaabat_1ph: A new public front-end to the MELTS, pMELTS, and pHMELTS models. *Geochemistry, Geophysics, Geosystems*, 6, Q02004. <https://doi.org/10.1029/2004GC000816>
- Smythe, D. J., & Brenan, J. M. (2016). Magmatic oxygen fugacity estimated using zircon-melt partitioning of cerium. *Earth and Planetary Science Letters*, 453, 260–266. <https://doi.org/10.1016/j.epsl.2016.08.013>
- Speer, J. A. (1984). Micas in igneous rocks. *Reviews in Mineralogy and Geochemistry*, 13(1), 299–356.
- Stepanov, A. S., Hermann, J., Rubatto, D., & Rapp, R. P. (2012). Experimental study of monazite/melt partitioning with implications for the REE, Th and U geochemistry of crustal rocks. *Chemical Geology*, 300, 200–220. <https://doi.org/10.1016/j.chemgeo.2012.01.007>
- Sun, S. S., & McDonough, W. F. (1989). Chemical and isotopic systematics of oceanic basalts: Implications for mantle composition and processes. *Geological Society, London, Special Publications*, 42, 313–345. <https://doi.org/10.1144/GSL.SP.1989.042.01.19>
- Taylor, S. R., & McLennan, S. M. (1985). *The Continental Crust: Its Composition and Evolution*. London: Blackwell Scientific Publications.
- Thomas, J. B., Bodnar, R. J., Shimizu, N., & Sinha, A. K. (2002). Determination of zircon/melt trace element partition coefficients from SIMS analysis of melt inclusions in zircon. *Geochimica et Cosmochimica Acta*, 66(16), 2887–2901. [https://doi.org/10.1016/S0016-7037\(02\)00881-5](https://doi.org/10.1016/S0016-7037(02)00881-5)
- Trail, D., Tailby, N. D., Lanzirrotti, A., Newville, M., Thomas, J. B., & Watson, E. B. (2015). Redox evolution of silicic magmas: Insights from XANES measurements of Ce valence in Bishop Tuff zircons. *Chemical Geology*, 402, 77–88. <https://doi.org/10.1016/j.chemgeo.2015.02.033>
- Trail, D., Watson, E. B., & Tailby, N. D. (2011). The oxidation state of Hadean magmas and implications for early Earth's atmosphere. *Nature*, 480(7375), 79–82. <https://doi.org/10.1038/nature10655>
- Trail, D., Watson, E. B., & Tailby, N. D. (2012). Ce and Eu anomalies in zircon as proxies for the oxidation state of magmas. *Geochimica et Cosmochimica Acta*, 97, 70–87. <https://doi.org/10.1016/j.gca.2012.08.032>
- Uchida, E., Endo, S., & Makino, M. (2007). Relationship between solidification depth of granitic rocks and formation of hydrothermal ore deposits. *Resource Geology*, 57(1), 47–56. <https://doi.org/10.1111/j.1751-3928.2006.00004.x>
- van Rossum, G., & Drake, F. L. Jr. (1995). *Python Tutorial*. Amsterdam, The Netherlands: Centrum voor Wiskunde en Informatica.
- van Rossum, G., & Drake, F. L. (2011). *The python language reference manual*. Network Theory Ltd.
- Venezky, D. Y., & Rutherford, M. J. (1999). Petrology and Fe-Ti oxide reequilibration of the 1991 Mount Unzen mixed magma. *Journal of Volcanology and Geothermal Research*, 89(1-4), 213–230. [https://doi.org/10.1016/S0377-0273\(98\)00133-4](https://doi.org/10.1016/S0377-0273(98)00133-4)
- Waldbaum, D. R., & Thompson, J. B. Jr. (1969). Mixing properties of sanidine crystalline solutions: IV. Phase diagrams from equations of state. *American Mineralogist*, 54(9-10), 1274–1298.

- Wang, R., Richards, J. P., Hou, Z. Q., Yang, Z. M., Gou, Z. B., & DuFrane, S. A. (2014). Increasing magmatic oxidation state from Paleocene to Miocene in the Eastern Gangdese Belt, Tibet: Implication for collision-related porphyry Cu–Mo–Au mineralization. *Economic Geology*, *109*(7), 1943–1965. <https://doi.org/10.2113/econgeo.109.7.1943>
- Watson, E. B., & Harrison, T. M. (1983). Zircon saturation revisited: Temperature and composition effects in a variety of crustal magma types. *Earth and Planetary Science Letters*, *64*(2), 295–304. [https://doi.org/10.1016/0012-821X\(83\)90211-X](https://doi.org/10.1016/0012-821X(83)90211-X)
- Watson, E. B., Wark, D. A., & Thomas, J. B. (2006). Crystallization thermometers for zircon and rutile. *Contributions to Mineralogy and Petrology*, *151*(4), 413. <https://doi.org/10.1007/s00410-006-0068-5>
- Wones, D. R. (1972). Stability of biotite: A reply. *American Mineralogist*, *57*(1–2), 316–317.
- Wones, D. R. (1981). Mafic silicates as indicators of intensive variables in granitic magmas. *Mining Geology*, *31*(168), 191–212. <https://doi.org/10.11456/shigenchishitsu1951.31.191>
- Wones, D. R., & Eugster, H. P. (1965). Stability of biotite—experiment theory and application. *American Mineralogist*, *50*(9), 1228–1272.
- Woodland, A. B., & Wood, B. J. (1994). Fe₃O₄ activities in Fe–Ti spinel solid solutions. *European Journal of Mineralogy*, *6*, 23–37. <https://doi.org/10.1127/ejm/6/1/0023>
- Yang, Z. M., Goldfarb, R., & Chang, Z. S. (2016). Generation of postcollisional porphyry Cu deposits in southern Tibet triggered by subduction of Indian continental plate. *Society of Economic Geologists Special Publication*, *19*, 279–300. <https://doi.org/10.5382/SP.19.11>
- Yavuz, F. (2003a). Evaluating micas in petrologic and metallogenic aspect: I—Definitions and structure of the computer program MICA+. *Computers & Geosciences*, *29*(10), 1203–1213. [https://doi.org/10.1016/S0098-3004\(03\)00142-0](https://doi.org/10.1016/S0098-3004(03)00142-0)
- Yavuz, F. (2003b). Evaluating micas in petrologic and metallogenic aspect: Part II—Applications using the computer program Mica+. *Computers & Geosciences*, *29*(10), 1215–1228. [https://doi.org/10.1016/S0098-3004\(03\)00143-2](https://doi.org/10.1016/S0098-3004(03)00143-2)
- Yavuz, F., & Öztaş, T. (1997). BIOTERM—A program for evaluating and plotting microprobe analyses of biotite from barren and mineralized magmatic suites. *Computers & Geosciences*, *23*(8), 897–907. [https://doi.org/10.1016/S0098-3004\(97\)00071-X](https://doi.org/10.1016/S0098-3004(97)00071-X)
- Zajacz, Z., Seo, J. H., Candela, P. A., Piccoli, P. M., & Tossell, J. A. (2011). The solubility of copper in high-temperature magmatic vapors: A quest for the significance of various chloride and sulfide complexes. *Geochimica et Cosmochimica Acta*, *75*(10), 2811–2827. <https://doi.org/10.1016/j.gca.2011.02.029>
- Zou, X., Qin, K., Han, X., Li, G., Evans, N. J., Li, Z., & Yang, W. (2019). Insight into zircon REE oxy-barometers: A lattice strain model perspective. *Earth and Planetary Science Letters*, *506*, 87–96. <https://doi.org/10.1016/j.epsl.2018.10.031>